On the Mechanics of Bioimpedance Signals Under Deformation

Chihtong Lee (cl124@rice.edu)
Department of Mechanical Engineering, Rice University, Houston, Texas, 77005

William Chan Santos (wjc83@miami.edu)
Department of Mechanical Engineering, Rice University, Houston, Texas, 77005
Department of Mechanical and Aerospace Engineering, University of Miami, Coral Gables, Florida, 33146

Carmina Andrade (ca77@rice.edu)
Department of Mechanical Engineering, Rice University, Houston, Texas, 77005

Raudel Avila (ra88@rice.edu)
Department of Mechanical Engineering, Rice University, Houston, Texas, 77005
Rice Advanced Materials Institute, Rice University, Houston, Texas, 77005
Rice Brain Institute, Rice University, Houston, Texas, 77005
Ken Kennedy Institute, Rice University, Houston, Texas, 77005

Corresponding Author: Raudel Avila (ra88@rice.edu)

Abstract

Bioimpedance provides a noninvasive means of characterizing biological tissues and monitoring physiological function. In wearable and skin-integrated systems, however, electrical measurements are acquired while the underlying tissues undergo extension, bending, twisting, compression, and physiological motion. These deformations alter the conducting domain, electrode placement, and redistribute the three-dimensional current field. The measured impedance, therefore, reflects both the tissue's electrical properties and its mechanical state, yet the mechanics governing this dependence remain poorly understood. Here, we combine tetrapolar measurements on conductive hydrogel phantoms, coupled mechanics and electrical finite element analysis, and reduced-order theory to determine how distinct deformation modes enter the impedance response. Deformation alone produces systematic impedance changes reaching approximately 30% under extension, 5% under bending, and 3% under torsion. These relations reproduce the experimental means with root-mean-square errors below 1.2 percentage points and demonstrate that response magnitude is governed by the order at which deformation perturbs electrically weighted current paths, rather than by the apparent complexity of the deformation field. Finite element calculations further show that, for uniform and variable conductivity, conductivity sets the absolute impedance scale while deformation produces a distinct normalized geometric offset. Small conductivity uncertainties can nevertheless equal or exceed the complete bending and torsional signals, and this separation breaks down when conductivity varies spatially or evolves during deformation. These findings establish mechanics as a governing state variable in bioimpedance and provide a basis for distinguishing deformation-induced signals from physiological changes in wearable measurements of highly deformable tissues.

Keywords
Bioimpedance
Mechanics
Hydrogels
Wearable Devices
Finite Element Analysis

Introduction

Bioimpedance provides a noninvasive means to interrogate the electrical properties of biological tissues and has become an important tool for physiological monitoring [1,2], disease diagnosis [3,4], and therapeutic guidance [5]. The emergence of wearable and implantable bioelectronics has further expanded its use by enabling continuous electrical measurements directly at the tissue interface [6–9]. Beyond these applications, bioimpedance is increasingly used to interrogate compliant organs, including the breast during milk pumping [10], the thorax during respiration [11–13], and soft tissues subjected to palpation [14] or external loading [15]. In each of these examples, electrical measurements are acquired while the underlying tissue undergoes non-negligible deformation.

Conventional interpretations of bioimpedance primarily attribute changes in the measured electrical response to variations in tissue composition or intrinsic electrical properties [16]. Mechanical deformation, however, simultaneously transforms the geometry on which the electrical boundary-value problem is defined by altering tissue dimensions, electrode spacing, and the distribution of electrical current. Consequently, the measured impedance reflects not only the constitutive electrical properties of the tissue but also its deformed configuration [17,18]. Without accounting for these geometric effects, changes arising solely from deformation may be incorrectly attributed to variations in tissue electrical properties or the underlying physiology. Although this electromechanical coupling is intrinsic to bioimpedance measurements performed on soft biological systems, its influence remains largely unexplored, and deformation is commonly minimized, corrected, or otherwise removed rather than quantified as part of the measurement itself. As bioimpedance technologies continue to transition toward soft, skin-integrated platforms, understanding the role of deformation becomes increasingly important for the interpretation of electrical measurements.

Electrical measurements acquired from deformable biological tissues cannot, in general, be interpreted independently of the underlying tissue mechanics. The central question addressed in this work is therefore not whether deformation influences bioimpedance, but under what conditions deformation becomes a governing contributor to the measured electrical response. Answering this question establishes the basis for distinguishing mechanical changes from intrinsic variations in tissue electrical properties and enables the interpretation of bioimpedance measurements acquired under conditions where deformation is inherent to tissue function.

2 Bioimpedance of Conductive Media Under Deformation

Figure 1A illustrates the three modes of deformation investigated experimentally: uniaxial extension, cylindrical bending, and torsion. These loading conditions were selected because they span the principal kinematic states experienced by skin-integrated bioelectronic systems and deformable soft tissues during physiological motion represented here on a homogeneous conductive hydrogel (conductivity ~0.5 S m^{-1}, dimensions 20 cm x 20 cm x 0.5 cm) instrumented with a linear tetrapolar array of four Ag/AgCl wet electrodes (Kendall Medi-Trace, 200 Series). Although each mode preserves the intrinsic electrical properties of the conductive medium, they modify the electrical boundary-value problem through distinct geometric mechanisms through which electrical current propagates between the source and sensing electrodes. Figure 1B presents the corresponding three-dimensional (3D) finite element simulations of the true strain within the conductive substrate. The 3D simulations establish the distinct deformation fields associated with each loading condition and provide the mechanical basis for interpreting the measured electrical response. Although all three loading conditions deform the same conductive material, they produce fundamentally different geometric perturbations of the electrical problem.

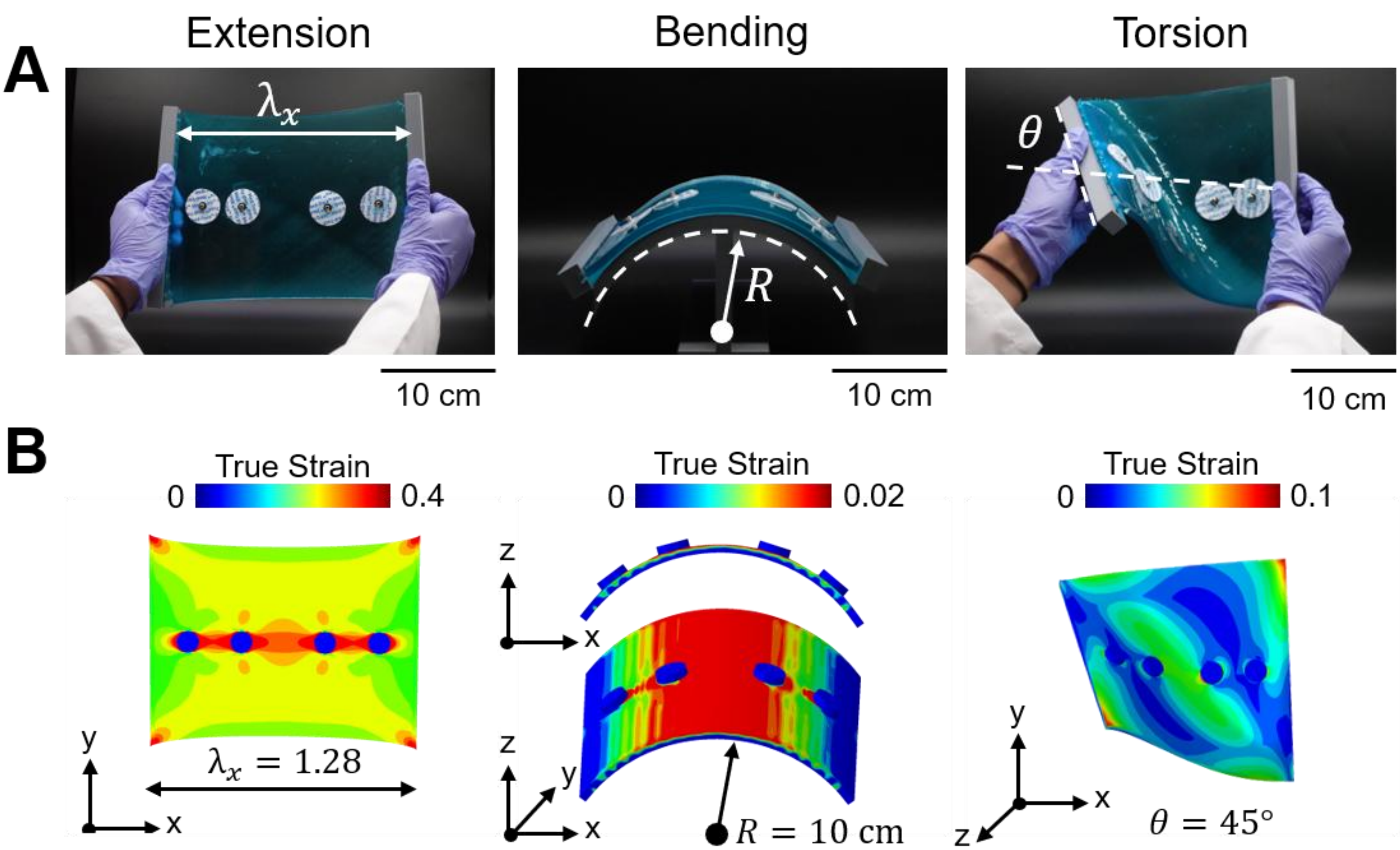

Figure 1 Experimental and finite element modeling of the three deformation modes. (**A**) Conductive hydrogel specimens under uniaxial extension, cylindrical bending, and twisting, characterized by the axial stretch $\lambda_x = L/L_0$, bending radius R, and twist angle θ, respectively. (Scale bars 10 cm). (**B**) Corresponding finite element distributions of true strain in the conductive hydrogel under $\lambda_x = 1.28$, bending radius $R = 10\ \mathrm{cm}$, and twist angle $\theta = 45°$.

2.1 Reduced-Order Model of Bioimpedance Under Deformation

Consider the tetrapolar transfer impedance

$$\tilde{Z}_{14,23} = \frac{\tilde{V}_2 - \tilde{V}_3}{\tilde{I}_{14}} \quad (1)$$

where electrodes 1 and 4 inject current and electrodes 2 and 3 measure the resulting potential difference. At a fixed angular frequency ω, the complex conductivity and resistivity are

$$\tilde{\sigma}(\omega) = \sigma(\omega) + j\omega\varepsilon(\omega) \quad (2.1)$$

$$\tilde{\rho}(\omega) = \tilde{\sigma}^{-1}(\omega) \quad (2.2)$$

The complete transfer impedance follows from the three-dimensional electro quasistatic boundary-value problem. To isolate the geometric effect of deformation, the electrically sampled region is reduced to an effective material current tube extending between the voltage electrodes. Let S denote its reference arc-length coordinate, A_0 its undeformed cross-sectional area, and $\mathbf{M}$ its unit tangent. Under the deformation $\mathbf{x} = \boldsymbol{\chi}(\mathbf{X})$, define

$$\mathbf{F} = \frac{\partial \mathbf{x}}{\partial \mathbf{X}} \quad (3.1)$$

$$\mathbf{C} = \mathbf{F}^{\mathrm{T}}\mathbf{F} \quad (3.2)$$

$$J = \det\mathbf{F} \quad (3.3)$$

The stretch of the current path is

$$\Lambda = \frac{ds}{dS} = \sqrt{\mathbf{M} \cdot \mathbf{C}\mathbf{M}} \quad (4)$$

Application of Nanson's relation to a material cross section initially normal to $\mathbf{M}$ gives its projected area normal to the deformed current path as

$$A = \frac{J}{\Lambda} A_0 \quad (5)$$

The incremental impedance of the idealized current tube is therefore

$$d\tilde{Z} = \tilde{\rho}\frac{ds}{A} = \frac{\tilde{\rho}}{A_0}\frac{\Lambda^2}{J}\,dS \tag{6}$$

For spatially uniform deformation

$$\frac{\tilde{Z}}{\tilde{Z}_0} = \frac{\tilde{\rho}}{\tilde{\rho}_0}\frac{\Lambda^2}{J} \tag{7}$$

Neglecting changes in the intrinsic electrical properties, $\tilde{\rho} = \tilde{\rho}_0$. The nearly incompressible response of the conductive hydrogel further gives $J \simeq 1$, such that

$$\frac{\tilde{Z}}{\tilde{Z}_0} = \Lambda^2 \tag{8}$$

Because the multiplicative geometric factor in Eq. (7) is real, the same scaling applies to both the complex impedance and its magnitude. The three loading modes differ through the kinematics that determine Λ. The undeformed impedance $\tilde{Z}_0$ differed by up to approximately 5% among hydrogel specimens, primarily because of small variations in electrode position and finite contact geometry introduced during manual assembly. These offsets are comparable in magnitude to the bending and torsional responses and therefore cannot be neglected. Normalization by the specimen-specific value of $\tilde{Z}_0$ removes this baseline variability from the comparison of the deformation responses as explained in the following sections.

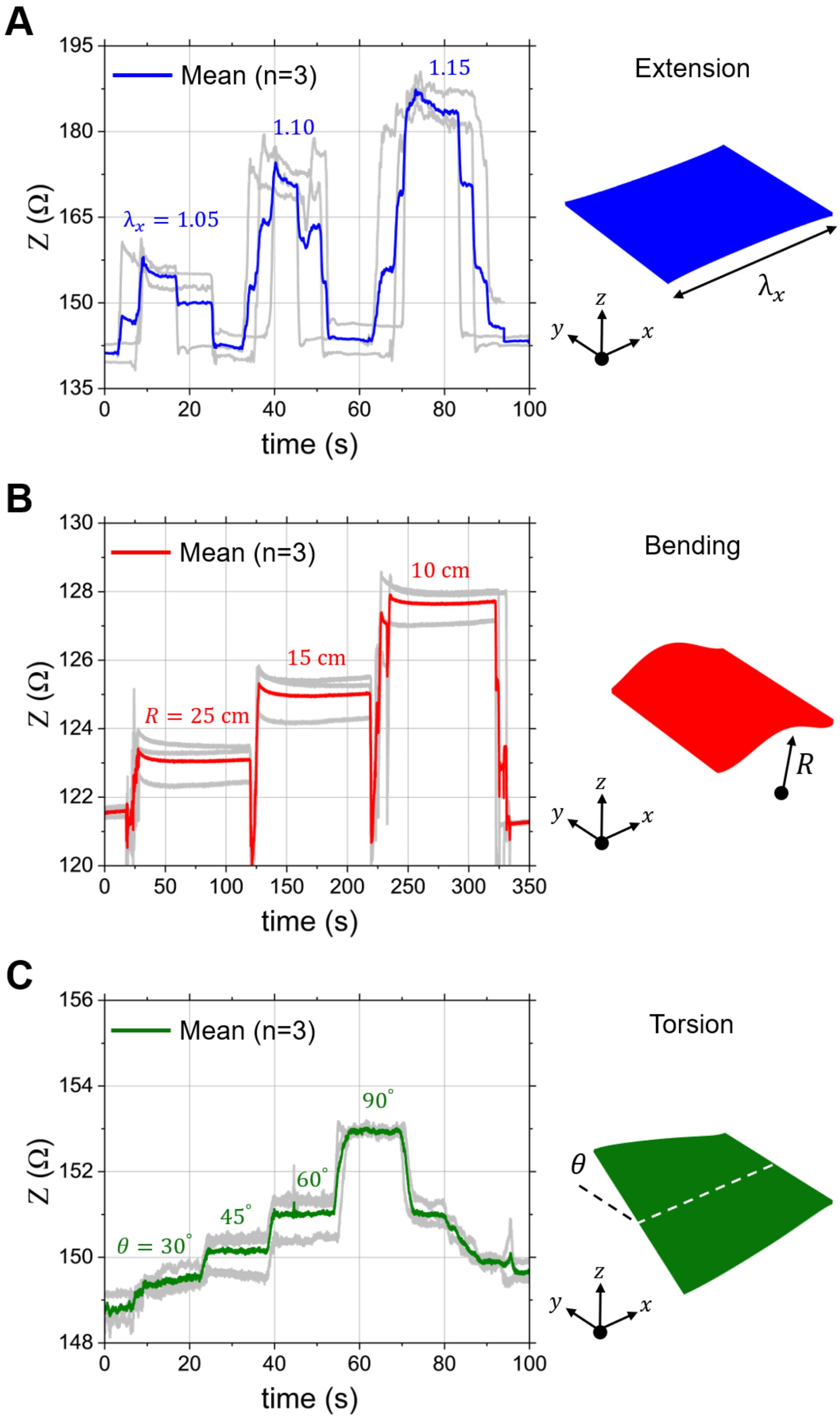

Figure 2. Temporal evolution of bioimpedance magnitude, Z, during stepwise (A) uniaxial extension, (B) bending, and (C) torsion. Prescribed deformation levels are identified by the axial stretch ratio λ_x, bending radius R, and twist angle θ, respectively. Gray curves represent three independent measurements for each loading mode; colored curves denote their pointwise mean ($\mathrm{n} = 3$). Schematics illustrate the corresponding deformed configurations and loading parameters.

2.2 Uniaxial Extension

Figure 2A shows the evolution of the normalized tetrapolar impedance during cyclic uniaxial extension. Three independent measurements were performed using separate conductive hydrogel specimens, with the ensemble mean shown in blue and the individual responses shown in gray. Increasing the axial stretch from $\lambda_x = 1$ to 1.05, 1.10, and 1.15 produces mean impedance changes of $9.75 \pm 2.48\%$, $21.64 \pm 2.52\%$, and $30.47 \pm 1.24\%$, respectively. Across the stretch range investigated, the transfer impedance increases from approximately 140 Ω to 183 Ω. The loading and unloading branches nearly coincide, indicating limited hysteresis and negligible residual change following removal of the applied deformation.

For an incompressible substrate subjected to homogeneous uniaxial extension along the electrode direction, the deformation gradient is

$$\mathbf{F}_s = \mathrm{diag}\left(\lambda_x, {\lambda_x}^{-1/2}, {\lambda_x}^{-1/2}\right) \tag{9.1}$$

$$J = \det\mathbf{F}_s = 1 \tag{9.2}$$

The reduced-order current-path model then gives

$$\frac{\tilde{Z}}{\tilde{Z}_0} = \lambda_x^2 \tag{10}$$

or, with $\lambda_x = 1 + \epsilon$,

$$\frac{\Delta Z_S}{Z_0} = (1+\epsilon)^2 - 1 = 2\epsilon + \epsilon^2 \tag{11}$$

One factor of λ_x arises from elongation of the characteristic current path, whereas the second arises from the reduction of its effective conducting cross-sectional area,

$$\frac{A}{A_0} = \lambda_x^{-1} \tag{12}$$

The predicted impedance changes from stretch ratios of 1.05, 1.10, and 1.15 are 10.25%, 21.00%, and 32.25%, respectively. These parameter-free predictions agree closely with the experimental means, with a root-mean-square error of approximately 1.1 percentage points.

The monotonic increase in impedance is therefore consistent with the finite-deformation kinematics of an approximately incompressible conductive domain. The recovery of Z_0 following unloading, together with the agreement between the measurements and the geometric scaling, indicates that deformation of the current path provides the leading-order contribution over the investigated stretch range. The measurements alone, however, do not exclude smaller deformation-dependent changes in the intrinsic conductivity of the hydrogel.

2.3 Bending

Figure 2B shows the impedance response under bending. Three independent measurements were performed using separate conductive hydrogel specimens, with the ensemble mean shown in red and the individual responses shown in gray. Decreasing the bending radius ρ from 25 cm to 15 cm and 10 cm, corresponding to increasing curvatures κ of 0.04 cm^{-1}, ~0.06 cm^{-1}, and 0.1 cm^{-1}, produces mean impedance changes of $1.23 \pm 0.55\%$, $2.81 \pm 0.56\%$, and $5.02 \pm 0.48\%$, respectively. The response is substantially smaller than that produced by uniaxial extension but increases monotonically with curvature. For a substrate of thickness $h = 5$ mm, the dimensionless curvature varies from $\kappa h = 0.02$ at $R = 25$ cm to $\kappa h = 0.05$ at $R = 10$ cm. Under pure bending, the longitudinal stretch of a material fiber located a distance z from the neutral surface is

$$\Lambda_b(z) = 1 + \kappa z \tag{13}$$

Bending therefore generates tensile and compressive regions separated by a neutral surface, rather than the approximately homogeneous strain field produced by uniaxial extension. If the electrical field sampled the substrate symmetrically through its thickness, the first-order contributions from the tensile and compressive regions would cancel. The surface-mounted electrode configuration instead produces an asymmetric lead field biased toward the electrode-bearing surface. The corresponding reduced-order response can be expressed as

$$\frac{\Delta Z_B}{Z_0} = 2\kappa \bar{z}_w + \kappa^2 \overline{z^2}_w \tag{14}$$

where $\bar{z}_w$ and $\bar{z^2}_w$ denote the first and second moments of depth weighted by the electrical sensitivity field.

When the sensitivity field is concentrated near a single effective depth z_{eff}, this expression reduces to

$$\frac{\Delta Z_B}{Z_0} \approx (1 + \kappa z_{\mathrm{eff}})^2 - 1 = \left(1 + \frac{z_{\mathrm{eff}}}{R}\right)^2 - 1 \tag{15}$$

A least-squares comparison with the measurements gives

$$z_{\mathrm{eff}} = 2.275\,\mathrm{mm} = 0.91\frac{h}{2} \tag{16}$$

This value lies within the geometric bound

$$0 \leq z_{\mathrm{eff}} \leq \frac{h}{2} \tag{17}$$

and is close to the electrode-bearing surface. The resulting correlation predicts impedance changes of 1.83%, 3.06%, and 4.60% at radii of 25, 15, and 10 cm, respectively. The model captures both the magnitude of the response and its inverse dependence on radius. The larger discrepancy at $\rho = 25$cm indicates, however, that a single effective depth does not fully represent the three-dimensional redistribution of electrical current throughout the specimen.

The positive response that is approximately linear in κ is therefore associated with the nonzero first moment $\bar{z}_w$ of the electrical sensitivity field. Curvature enters the impedance not simply by changing the distances between electrodes but by coupling the through-thickness strain gradient to the spatial distribution of electrical current. For $\kappa h \ll 1$, the leading-order response is

$$\frac{\Delta Z_B}{Z_0} \simeq 2\kappa z_{\mathrm{eff}} \tag{18}$$

demonstrating that bending scales impedance linearly with curvature.

2.4 Torsion

Figure 2C shows the impedance response under torsional deformation. Three independent measurements were performed using separate conductive hydrogel specimens, with the ensemble mean shown in green and the individual responses shown in gray. Increasing the total twist angle from $0°$to $30°$, $45°$, $60°$, and $90°$produces mean impedance changes of $0.45 \pm 0.25\%$, $0.93 \pm 0.24\%$, $1.52 \pm 0.22\%$, and $2.81 \pm 0.26\%$, respectively. Torsion produces the smallest impedance change among the three deformation modes despite generating the most spatially heterogeneous strain field.

For a specimen twisted uniformly over a gauge length L_t, the twist rate is

$$\psi = \frac{\theta}{L_t} \tag{19}$$

where θ is expressed in radians. Neglecting cross-sectional warping, a longitudinal material path located a radial distance r from the twisting axis follows a helical trajectory with stretch

$$\Lambda_t^2(r) = 1 + \psi^2 r^2 \tag{20}$$

Averaging over the electrically sampled region gives

$$\frac{\Delta Z_T}{Z_0} = \left(\frac{r_{\mathrm{eff}}\theta}{L_t}\right)^2 \tag{21.1}$$

$$r_{\mathrm{eff}}^2 = \overline{r^2}_w \tag{21.2}$$

where r_{eff} is the sensitivity-weighted root-mean-square distance from the twisting axis. For $L_t = 200$ mm, comparison with the measurements gives

$$\frac{r_{\mathrm{eff}}}{L_t} = 0.1097, \qquad r_{\mathrm{eff}} = 21.9\,\mathrm{mm}, \tag{22}$$

The resulting correlation predicts impedance changes of 0.33%, 0.74%, 1.32%, and 2.97% at $30°$, $45°$, $60°$, and $90°$, respectively, with a root-mean-square error of approximately 0.17 percentage points. The torsional response is quadratic because the extension of a helical material path depends on $\psi^2 r^2$. Consequently, no term linear in θ is permitted by symmetry, and the reduced-order model predicts identical leading-order responses for positive and negative twisting. The comparatively small, measured impedance change is therefore consistent with the second-order character of the torsional path extension, rather than with an absence of mechanically induced current redistribution.

2.5 Deformation Dependent Asymptotic Orders

Taken together, the three deformation modes reveal distinct asymptotic orders of the deformation-induced impedance response:

$$\frac{\Delta Z}{Z_0} = \begin{cases} O(\epsilon), & \text{extension} \\ O(\kappa z_{\mathrm{eff}}), & \text{bending} \\ O\left[\left(\frac{r_{\mathrm{eff}}\theta}{L_t}\right)^2\right], & \text{torsion} \end{cases} \tag{23}$$

This hierarchy explains why uniaxial extension produces an impedance change of approximately 30%, whereas bending and torsion produce maximum changes of approximately 5% and 3%, respectively. The relative magnitudes are governed by the kinematic order of the electrically sampled path stretch, rather than by the apparent complexity of the macroscopic deformation field. These results establish deformation as a leading-order contributor to the measured bioimpedance and demonstrate that the mechanical configuration must be quantified when interpreting electrical measurements obtained from deformable substrates and soft biological tissues. The three deformation modes are summarized as

$$\frac{\Delta Z}{Z_0}(\%) = \begin{cases} 100[(1+\epsilon)^2 - 1], & \text{extension} \\ 100\left[\left(1 + \frac{z_{\mathrm{eff}}}{R}\right)^2 - 1\right], & \text{bending} \\ \left(\frac{r_{\mathrm{eff}}}{L_t}\right)^2 \left(\frac{\pi}{180}\right)^2 \theta_{\mathrm{deg}}^2, & \text{torsion} \end{cases} \tag{24}$$

2.6 Mechanics Governing the Impedance Response

Figure 3 compares experimental measurements with the three-dimensional finite element calculations and the reduced-order theory developed in the preceding section. The purpose of this comparison is not merely to establish numerical agreement. Rather, it is to determine which features of the deformation field survive the spatial averaging inherent to a tetrapolar impedance measurement. The experiments provide the net electrical response, the finite element calculations resolve the deformed geometry and three-dimensional current redistribution, and the theory identifies the kinematic quantity that enters at leading order. The reduced-order results obtained above have the asymptotic forms

$$\frac{\Delta Z}{Z_0} \sim \begin{cases} 2\epsilon + O(\epsilon^2), & \text{extension} \\ 2\kappa z_{\mathrm{eff}} + O[(kh)^2], & \text{bending} \\ \left(\frac{r_{\mathrm{eff}}\theta}{L_t}\right)^2 + O\left[\left(\frac{r_{\mathrm{eff}}\theta}{L_t}\right)^4\right], & \text{torsion} \end{cases} \tag{25}$$

Extension produces a first-order response throughout the conductive domain. Bending produces a first-order response only because the electrodes break the symmetry about the neutral surface. Torsion admits no term linear in θ; reversal of the twist direction leaves the leading path length unchanged, and the response must therefore begin at second order. The relevant nondimensional measures reach

$$\epsilon_{\max} = 0.15 \tag{26.1}$$

$$(kh)_{\max} = 0.05 \tag{26.2}$$

$$\left(\frac{r_{\mathrm{eff}}\theta}{L_t}\right)_{\max} = 0.172 \qquad (26.3)$$

Thus, even though the specimen undergoes a total twist of $90°$, the electrically sampled helical extension remains small. The most heterogeneous deformation field does not necessarily produce the largest impedance change; the controlling question is the order at which that field changes the electrically weighted conducting paths.

Under uniaxial extension (Figure 3A), strains of 5%, 10%, and 15% produce experimental impedance changes of 9.75 ± 2.48%, 21.64 ± 2.52%, and 30.47 ± 1.24%, respectively. The reduced-order theory predicts 10.25%, 21.00%, and 32.25%, giving a root-mean-square difference of 1.13 percentage points. This agreement is the most stringent of the three comparisons because the extension relation contains no fitted parameter. The leading term, 2ϵ, has a direct mechanical interpretation: one contribution arises from elongation of the conducting path and the other from transverse contraction of the nearly incompressible medium. At $\epsilon = 0.15$, this term alone gives a 30% increase, accounting for nearly the entire measured response. The finite-strain correction, ϵ^2, contributes an additional 2.25 percentage points to the theoretical prediction. The slightly smaller experimental value at the largest strain suggests that three-dimensional redistribution of current partially relaxes the ideal current tube amplification represented by the quadratic correction. The agreement nevertheless establishes the first-order geometric gauge factor of two as the dominant behavior. The nominal-conductivity finite element calculations reproduce the monotonic increase with strain but underpredict its magnitude, with the separation increasing as the deformation grows. The conductivity-adjusted calculations restore close agreement with the experiment and theory. The important result is that all three descriptions recover the same first-order dependence on ϵ. The remaining difference lies primarily in the coefficient of the higher-order contribution, which is sensitive to finite electrode geometry, nonuniform current paths, and the electrical material scale.

Bending presents a fundamentally different asymptotic form (Figure 3B). The measured impedance changes are 5.02 ± 0.48%, 2.81 ± 0.56%, and 1.23 ± 0.55% at radii of 10, 15, and 25 cm, respectively. The reduced-order theory gives 4.60%, 3.06%, and 1.83%, with a root-mean-square difference of 0.45 percentage points. Although z_{eff} is obtained from Eq. (16), a single value reproduces the response over the full range of radii and, more importantly, satisfies the geometric bound imposed by the substrate thickness. The significance of this result is not the fit alone, but the location of the inferred length scale. Its proximity to $h/2$ shows that the electrical sensitivity is strongly weighted toward the electrode surface. Consequently, the tensile and compressive contributions do not cancel, and bending appears at first order through κz_{eff}. At the largest curvature, the leading contribution κz_{eff} gives 4.55%, whereas the quadratic correction contributes only approximately 0.05%. The measured bending response is therefore essentially a first-order curvature effect. This first-order term is not a universal consequence of bending: it exists because the lead field has a nonzero first moment about the neutral surface. A through-thickness symmetric electrode configuration would give $z_{\mathrm{eff}} = 0$, suppressing the linear term and reducing the leading response to $O[(kh)^2]$. Reversing the electrode surface from the tensile to the compressive side would reverse the sign of the linear contribution. Thus, the sign and magnitude of the bending response are jointly determined by curvature and electrode placement relative to the neutral surface.

The nominal-conductivity finite element results remain near over much of the investigated range and consequently fail to recover the observed decay with increasing radius. This nearly constant contribution is comparable to, or larger than, the bending signal itself and obscures the dependence. Conductivity adjustment restores the dependence of curvature and brings the calculations closer to the experiments. Bending therefore exposes an important limitation of forward electrical calculations: when the mechanically induced signal is only a few percent, a comparably small error in the electrical material scale can mask the leading mechanical dependence.

Torsion provides the clearest role of symmetry (Figure 3C). Twist angles of $30°$, $45°$, $60°$, and $90°$ produce experimental impedance changes of 0.45 ± 0.25%, 0.93 ± 0.24%, 1.52 ± 0.22%, and 2.81 ± 0.26%, respectively. The reduced-order theory gives 0.33%, 0.74%, 1.32%, and 2.97%, with a root-mean-square difference of 0.17 percentage points. The fitted value in Eq. (22) is substantially smaller than the specimen half-width of 100 mm. Hence, the electrical measurement does not uniformly sample the full torsion field. It is concentrated within a narrower region surrounding the electrode array, while the current can redistribute away from the more highly extended peripheral trajectories. The effective radius is therefore a sensitivity-weighted measure of the torsional field, not a geometric radius of the specimen. The finite element calculations recover the nonlinear increase with twist angle but overpredict its coefficient. At $90°$ the nominal-conductivity calculation approaches 8%, compared with the measured value of 2.81%. Conductivity adjustment substantially reduces this discrepancy, although the calculation remains above the measurements at the larger angles. The persistence of this difference suggests that the assumed electrical sensitivity field assigns excessive weight to regions of large radial displacement or that the modeled twist and electrode trajectories differ from those realized experimentally. The agreement of the experiments with the quadratic dependence, however, shows that the discrepancy concerns the effective coefficient—not the symmetry or leading order of the torsional response.

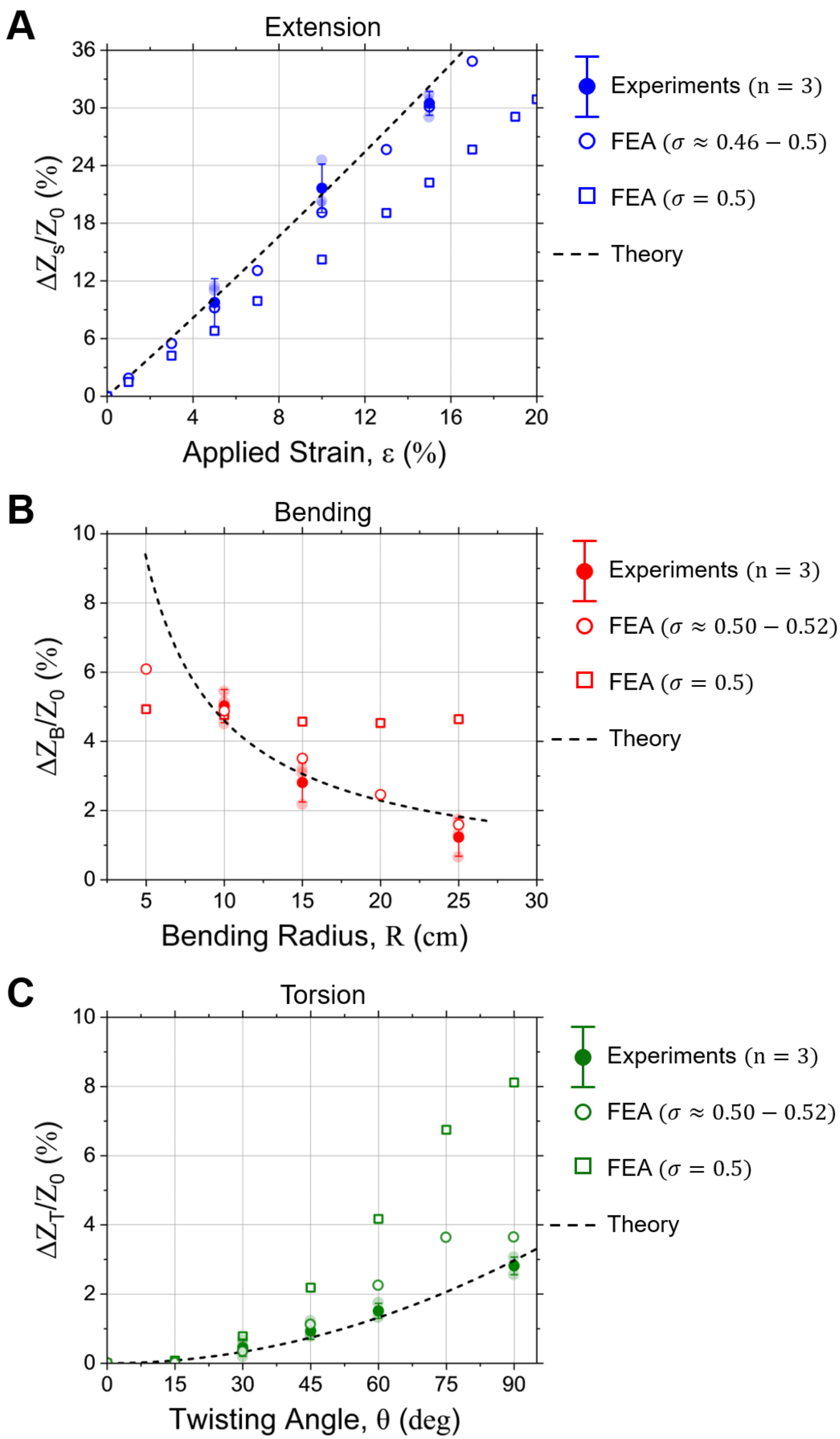

Figure 3. Experimental, computational, and theoretical dependence of normalized impedance change, $\Delta Z/Z_0$, on (A) applied strain during uniaxial extension, (B) bending radius, and (C) twist angle. Filled symbols and error bars denote the experimental mean ± standard deviation $(\mathrm{n} = 3)$; open circles denote finite-element predictions using conductivity calibrated to the undeformed impedance of each specimen, and open squares denote predictions obtained using a nominal conductivity, $\sigma = 0.5\ \mathrm{S/m}$. Dashed curves represent the reduced-order theoretical models.

2.7 Electric Field Redistribution and Conductivity Sensitivity

Figures 4 and 5 provide the field-level interpretation of the coupled mechanical and electrical response. Figure 4 shows that deformation does not merely alter a nominal distance between electrodes. It changes the shape of the conducting domain, transports and rotates the finite electrodes, and redistributes the electric field throughout the hydrogel. In every configuration, the largest field gradients remain concentrated near the electrode perimeters. The field connecting these localized regions, however, evolves with deformation: extension separates the electrodes and elongates the intervening field; bending curves the conducting domain and biases the field toward the electrode-bearing surface; and torsion rotates successive electrode, producing an oblique, fully three-dimensional electric field. The measured impedance is therefore a nonlocal consequence of the deformed domain and its electrical sensitivity field, rather than a local function of strain or electrode separation.

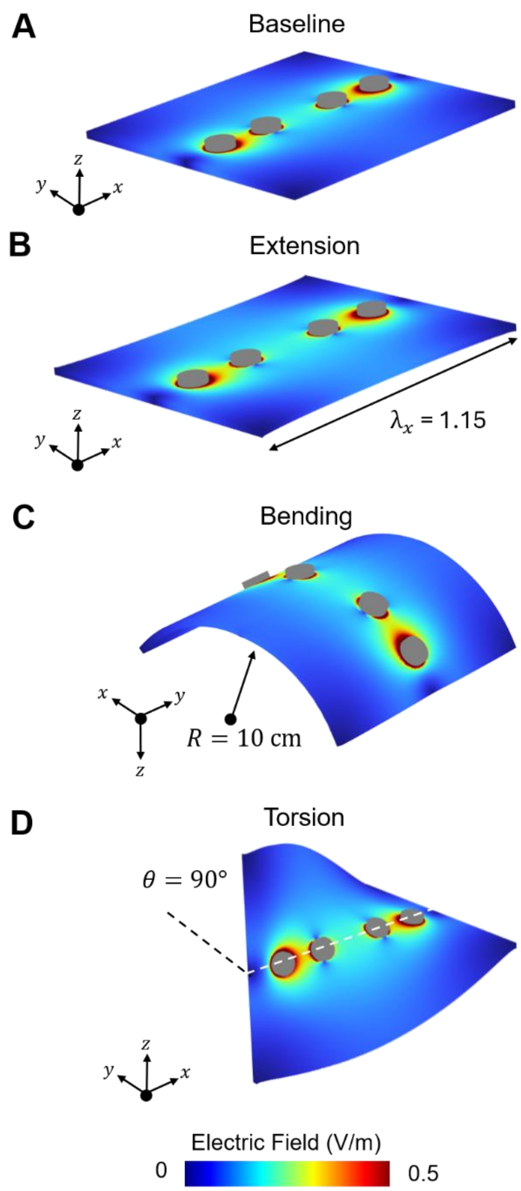

Figure 4. Redistribution of the electric-field magnitude within the conductive hydrogel for (A) the undeformed baseline and under (B) uniaxial extension ($\lambda_x = 1.15$), (C) bending ($R = 10\ \mathrm{cm}$), and (D) torsion ($\theta = 90°$). The deformed conductive geometry and corresponding changes in electrode position and orientation alter the spatial distribution of the electric field, with localization near the electrodes.

The parametric calculations in Figure 5 separate this geometric effect from the electrical material scale. At the measurement frequency of 50 kHz,

$$\frac{\omega\varepsilon}{\sigma} \approx 4.7 \times 10^{-4} \tag{27}$$

for $\varepsilon_r = 85$ and $\sigma = 0.5\,\mathrm{S\,m^{-1}}$, the response is dominated by conduction. For a spatially uniform conductivity, the impedance associated with deformation mode m can therefore be written approximately as

$$Z_m(\sigma) = \frac{\mathcal{G}_m}{\sigma} \tag{28}$$

where $\mathcal{G}_m$ is a geometric factor determined by the deformed domain, electrode configuration, and three-dimensional current distribution. The four nonintersecting curves in Figure 5 are the numerical confirmation of this separation. Increasing conductivity lowers the impedance of every configuration through the common $1/\sigma$ dependence, whereas deformation changes $\mathcal{G}_m$ and thereby displaces the corresponding branch from the undeformed baseline. For the representative maximum deformations shown ($\lambda_x = 1.15$, $\theta = 90°$, and $R = 10\,\mathrm{cm}$) each mode produces a distinct positive offset over the full conductivity range. Within the constant-conductivity model, their ordering is

$$\mathcal{G}_{\mathrm{extension}} > \mathcal{G}_{\mathrm{torsion}} > \mathcal{G}_{\mathrm{bending}} > \mathcal{G}_0 \tag{29}$$

The ordering reflects the current redistribution resolved by the finite element model; it is not prescribed through an electrode-spacing correction. Extension produces the largest separation because the deformation changes the field-bearing region coherently along the electrode direction. Bending and torsion produce smaller offsets because their heterogeneous deformation fields permit partial cancellation and redistribution toward less strongly extended conducting paths. An important consequence of the separable form is that, when the same uniform conductivity applies before and after deformation, the normalized impedance change is then independent of the absolute conductivity. Conductivity determines the electrical scale, while deformation determines the relative geometric offset.

The absolute separation,

$$Z_m - Z_0 = \frac{\mathcal{G}_m - \mathcal{G}_0}{\sigma} \tag{30}$$

decreases with increasing conductivity, as observed in Figure 5, but the corresponding normalized separation remains essentially unchanged. This explains why specimen-specific normalization by the undeformed impedance is effective when conductivity is spatially uniform and remains unchanged during loading. Figure 5 also exposes the sensitivity of any absolute comparison to the assigned conductivity. The uniform-conductivity model gives

$$\left.\frac{\partial\, \ln Z}{\partial\, \ln\sigma}\right|_{\mathcal{G}} = -1 \tag{31}$$

so that a 1% error in conductivity produces, to leading order, a 1% error of opposite sign in impedance. Over the interval $\sigma = 0.45$–$0.55\,\mathrm{S\,m^{-1}}$, the conductivity-induced displacement of the impedance is comparable to the complete bending and torsional signals. The extension response remains readily distinguishable because its geometric offset is large. For bending and torsion, however, a modest error in conductivity can equal or exceed the deformation-induced impedance change. Consequently, calculations using a single nominal value of σ may recover the correct dependence on deformation while failing to reproduce its absolute magnitude.

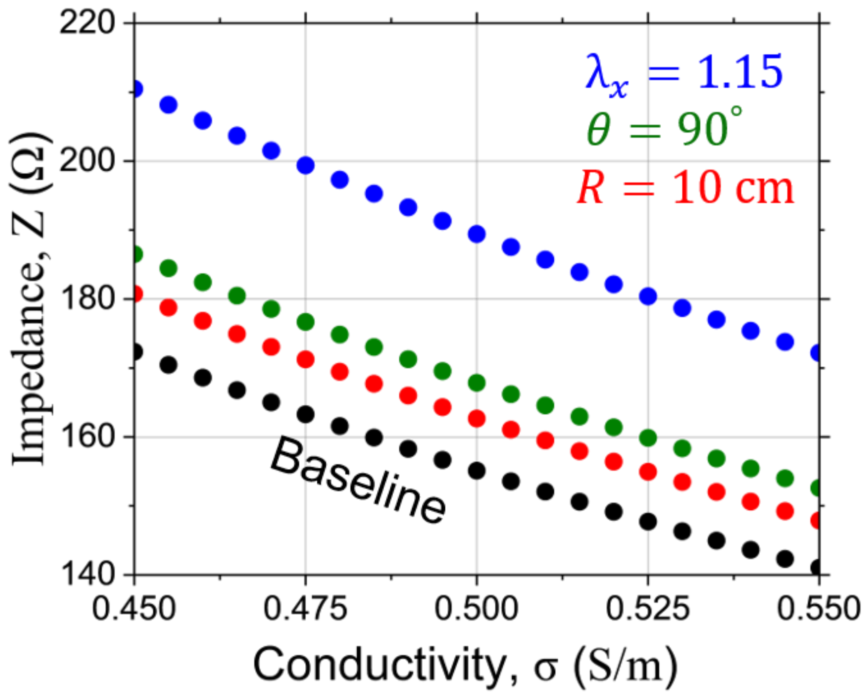

Figure 5. Influence of hydrogel conductivity, σ, on the impedance magnitude, Z, for the undeformed baseline and three representative deformation states: uniaxial extension ($\lambda_x = 1.15$), torsion ($\theta = 90°$), and bending ($R = 10$ cm). Impedance decreases with increasing conductivity for all configurations, while the separation of each deformed response from the baseline quantifies the contribution of deformation independently of conductivity.

Discussion and Future Outlook

Wearable bioimpedance systems are ultimately intended to monitor changes in tissue physiology. The present results demonstrate that routine physiological motion alone can generate impedance variations of comparable magnitude through deformation of the conductive domain [10,19]. Consequently, future bioimpedance platforms should quantify both mechanical deformation and electrical response to distinguish geometry-induced impedance changes from true physiological signals.

From a mechanics perspective, the central implication is that deformation is not an arbitrary motion artifact. Its contribution is structured by kinematics, symmetry, and the spatial sensitivity of the electrode configuration. This observation provides a useful design principle: if the electrode arrangement and conducting domain are symmetric with respect to a deformation mode, the first-order geometric contribution may vanish; when that symmetry is broken, the same deformation can enter at first order and dominate the measurement. Mechanics can therefore be used prospectively to determine which deformations a device will reject, detect, or amplify. This structure also exposes a fundamental identifiability problem. The measured impedance is a nonlocal functional of the conductivity field, deformed geometry, electrode trajectories, and contact conditions. A change in any one of these quantities may produce a similar electrical response. Baseline normalization reduces this ambiguity only when conductivity remains spatially uniform and unchanged during deformation. In living tissues, deformation may simultaneously alter perfusion, fluid distribution, ionic concentration, and electrode contact. Geometry and physiology then become coupled contributions rather than separable sources of impedance change. Increasing the fidelity of the electrical model alone cannot resolve this nonuniqueness; additional mechanical or electrical characterization are required.

These considerations suggest two complementary directions for future wearable device design. Devices intended to isolate physiology should suppress the first variation of impedance with respect to expected motions through mechanically symmetric electrode layouts, strain-isolating structures, or compensation based on measured strain, curvature, and electrode displacement. Conversely, deformation sensitive layouts could deliberately amplify selected mechanical modes, allowing bioimpedance to provide information about tissue motion, distension, or mechanical state. In both cases, the electrical sensitivity field should be treated as a design variable rather than intrinsic to electrode placement.

The present homogeneous hydrogel system was designed to isolate this geometric contribution and does not reproduce the heterogeneity, anisotropy, interfacial slip, or transport mechanisms present in living tissue. The next challenge is therefore a coupled inverse problem in which tissue kinematics and electrical properties are inferred together. Multichannel electrode arrays, frequency-dependent measurements, and co-located mechanical sensing could provide the independent information needed to separate changes in geometry, conductivity, and contact. Coupled finite deformation and electrical models would then serve not merely to correct motion artifacts, but to establish whether a measured signal is mechanically admissible for the inferred physiological change.

The broader opportunity is to move wearable bioimpedance from empirical signal interpretation toward mechanics informed measurement. A wearable bioimpedance electrode array does not interrogate electrical properties independently of the body on which it is placed; it interrogates an evolving conductor whose geometry and material state are inseparable. Recognizing this coupling provides both a criterion for rejecting deformation errors and a viable route for extracting additional physiological information from the mechanics state itself.

3 Methods

3.1 Bioimpedance measurement and calibration

Bioimpedance was measured using a MAX30009 BioZ analog front end (Analog Devices, Wilmington, MA, USA) in a tetrapolar configuration. The two outer electrodes supplied the excitation current, while the two inner electrodes measured the resulting differential voltage. A sinusoidal current with an RMS amplitude of $64.1\ \mu\mathrm{A}$ and a frequency of 50 kHz was applied in current-drive mode. The excitation current was established using an RMS digital-to-analog converter voltage of 354 mV and a range resistance of $5.525\ \mathrm{k}\Omega$, such that

$$I_{\mathrm{RMS}} = \frac{V_{\mathrm{DAC,RMS}}}{R_{\mathrm{Range}}} = \frac{354\ \mathrm{mV}}{5.525\ \mathrm{k}\Omega} = 64.1\ \mu\mathrm{A} \tag{32}$$

The transmit-amplifier range and bandwidth were set to *High*. The receive-chain gain was 10 V/V, and the in-phase and quadrature components were sampled at 195.25 samples/s. These acquisition settings were maintained across all specimens and deformation modes.

Before hydrogel testing, the measurement chain was calibrated at 50 kHz using a precision $100\ \Omega$ reference resistor connected across the electrode terminals. Gain, phase, and direct-current offset corrections were determined independently for the in-phase (I) and quadrature (Q) channels, as summarized in Table 1. The calibration coefficients were subsequently applied to the measured I and Q signals to obtain the corrected complex transfer impedance

$$Z(t) = \frac{V_{23}(t)}{I_{14}(t)} = Z'(t) + jZ''(t) \tag{33}$$

where I_{14} denotes the current applied through the two outer electrodes and V_{23} is the differential voltage measured between the two inner electrodes.

Table 1. Calibration coefficients for the MAX30009 measurement system at 50 kHz

Frequency	50 kHz
I-channel Gain	0.9374
Q-channel Gain	0.9362
I-phase Correction	-1.350°
Q-phase Correction	-1.332°
I-channel DC offset	-658.5 counts
Q-channel DC offset	-400.6 counts

3.2 Conductive-hydrogel fabrication

Conductive gelatin–glycerol hydrogels were prepared using a formulation adapted from [20]. Gelatin, glycerol, and water were combined at a mass ratio of 1:1.5:2.5. Sodium chloride was dissolved in the water at a nominal concentration of 2 wt% to produce a target electrical conductivity of 0.5 S m^{-1} . The chilled saline solution was added to 240-Bloom porcine gelatin powder (Knox), and the gelatin was allowed to bloom for 10 min. USP-grade glycerol was then added, and the mixture was heated to 50℃ under continuous stirring until fully dissolved. The solution was maintained at 50℃ for an additional 50 min while covered to limit evaporation and permit entrained air to escape before casting.

Rectangular specimens measuring 20 x 20 x 0.5 cm^3 were cast in custom three-dimensional-printed polylactic acid (PLA) molds. PLA gripping fixtures were embedded along two opposing edges of each specimen. Each grip consisted of a 20 x 1 x 0.5 cm^3 chamber containing uniformly distributed 0.3 x 0.3 x 0.5 cm^3 internal posts. During casting, the hydrogel filled the spaces surrounding the posts, forming a mechanical interlock between the hydrogel and the rigid PLA grips. This arrangement transferred the applied loads into the specimen without directly clamping or locally compressing the compliant hydrogel. The specimens were allowed to gel at room temperature (25 ℃) for 3 hours before electrode placement and testing.

Four Ag/AgCl electrodes (Kendall Medi-Trace, 200-Series) with an active diameter of $D_e = 20$ mm were positioned collinearly along the centerline of the hydrogel surface. The initial center-to-center electrode spacings were $s_{12} = 20$, $s_{23} = 40$, and $s_{34} = 20$ mm. The outer electrodes were connected to the current-drive terminals, and the inner electrodes were connected to the differential-voltage inputs.

3.3 Mechanical loading

Bioimpedance was recorded under three deformation modes: uniaxial extension, bending, and twisting. The imposed deformations were characterized by the engineering strain

$$\epsilon = \frac{L - L_0}{L_0} \tag{34}$$

the bending curvature

$$\kappa = \frac{1}{R} \tag{35}$$

and the twist angle θ, respectively, where L_0 is the initial specimen length and R is the prescribed bending radius. Bioimpedance was recorded continuously throughout loading, unloading, and recovery. Before each loading sequence, the hydrogel specimen was placed in its undeformed configuration on a flat, electrically insulating surface, and its impedance was recorded for 25 s. After unloading, the specimen was returned to the same undeformed configuration and monitored for an additional 25 s to quantify baseline recovery and temporal drift. The baseline impedance Z_0 was defined as the time-averaged impedance magnitude during the initial undeformed time interval.

3.4 Mechanical Finite Element Analysis

3D finite element analyses were performed in ABAQUS/Standard (2026, Dassault Systèmes) to determine the deformation fields produced by bending, twisting, and uniaxial extension. The 20 x 20 x 0.5 cm^3 hydrogel specimen was discretized using a structured mesh with approximately 70,000 eight-node hybrid brick elements (C3D8H). The hydrogel was modeled as a homogeneous, isotropic, nearly incompressible neo-Hookean solid with strain-energy density $W = C_{10}(\bar{I}_1 - 3) + D_1^{-1}(J - 1)^2$. The material parameters $C_{10} = 1.68$ MPa and $D_1 = 0.012$ MPa^{-1} were calculated from $E = 10$ MPa, based on the measured stiffness of the Knox gelatin formulation reported by [20], and $\nu = 0.49$. Geometric nonlinearity was enabled for all simulations. For uniaxial extension, one end was fixed and the opposite end was displaced to produce the desired engineering strain and lateral contraction was unconstrained. For bending, the specimen was first subjected to a ~5% uniaxial prestrain and then pressed against a rigid cylindrical surface of radius R using a uniformly distributed pressure of 0.05 MPa. Contact was modeled using finite sliding with hard normal contact and frictionless tangential behavior. For twisting, the two end surfaces were coupled to reference points located at the surface centroid. One end was fixed, while the opposite end was rotated from $0°$ to $90°$ about the longitudinal axis. Transverse translations and rotations were constrained at the rotating end, whereas axial translation remained free to prevent artificial axial loading.

3.5 Electrical Finite Element Analysis

The deformed hydrogel and electrode geometries obtained from the mechanical analyses were imported into COMSOL Multiphysics (version 6.4, COMSOL Inc.) and independently remeshed using approximately 5×10^5 tetrahedral elements. Frequency-domain electric-current analyses were performed at $f = 50$ kHz by solving

$$\begin{cases} \nabla \cdot \mathbf{J} = 0 \\ \mathbf{J} = (\sigma + j\omega\varepsilon_0\varepsilon_r)\mathbf{E} \\ \mathbf{E} = -\nabla \mathrm{V} \end{cases} \tag{36}$$

where V is the electric potential and $\omega = 2\pi f$. The hydrogel was modeled as a homogeneous, isotropic conductive dielectric with relative permittivity $\varepsilon_r = 85$. The electrodes were modeled as silver conductors with $\sigma_{\mathrm{Ag}} = 6.16 \times 10^7$ S/m. A current of $64.1\ \mu\mathrm{A}_{\mathrm{RMS}}$ was applied through one outer electrode (Terminal 1), and the opposing outer electrode was grounded (Terminal 4). The two inner electrodes were treated as floating equipotential surfaces (Terminal 2 and Terminal 3) with zero net current, consistent with the high-input-impedance voltage measurement. All remaining external surfaces were electrically insulated. Electrical simulations were performed using two spatially uniform, deformation-independent conductivity assignments. First, a nominal conductivity of 0.50 S/m, corresponding to the target hydrogel formulation, was applied to all deformation modes. Second, for comparisons of normalized impedance, effective conductivity was calibrated independently over the 0.45-0.55 S m^{-1} range for each specimen series by matching only its undeformed experimental impedance. This baseline calibration (Figure 3) yielded conductivities of 0.46 - 0.50 S m^{-1} for extension, 0.50 - 0.52 S m^{-1} for twisting, and 0.50 - 0.52 S m^{-1} for bending.

Acknowledgements

R.A. acknowledges support from the Rice Office of Research and the Rice Brain Institute DPRIT Seed Grant Program. W.C.S. acknowledges support from the American Heart Association Summer Undergraduate Research for Foreign Nationals (SURFN) Program (Grant No. 24IAUST1247747). C.L. and C.A. acknowledges support from the Rice Advanced Materials Institute Undergraduate Research Fellowship Program.

Conflict of Interest

There are no conflicts of interests.

Data Availability

All the data is included in the manuscript.

Figure Captions

Figure 1 Experimental and finite element modeling of the three deformation modes. (A) Conductive hydrogel specimens under uniaxial extension, cylindrical bending, and twisting, characterized by the axial stretch $\lambda_x = L/L_0$, bending radius R, and twist angle θ, respectively. (Scale bars 10 cm). (B) Corresponding finite element distributions of true strain in the conductive hydrogel under $\lambda_x = 1.28$, bending radius $R = 10\ \mathrm{cm}$, and twist angle $\theta = 45°$.

Figure 2. Temporal evolution of bioimpedance magnitude, Z, during stepwise (A) uniaxial extension, (B) bending, and (C) torsion. Prescribed deformation levels are identified by the axial stretch ratio λ_x, bending radius R, and twist angle θ, respectively. Gray curves represent three independent measurements for each loading mode; colored curves denote their pointwise mean $(\mathrm{n} = 3)$. Schematics illustrate the corresponding deformed configurations and loading parameters.

Figure 3. Experimental, computational, and theoretical dependence of normalized impedance change, $\Delta Z/Z_0$, on (A) applied strain during uniaxial extension, (B) bending radius, and (C) twist angle. Filled symbols and error bars denote the experimental mean ± standard deviation $(\mathrm{n} = 3)$; open circles denote finite-element predictions using conductivity calibrated to the undeformed impedance of each specimen, and open squares denote predictions obtained using a nominal conductivity, $\sigma = 0.5\ \mathrm{S/m}$. Dashed curves represent the reduced-order theoretical models.

Figure 4. Redistribution of the electric-field magnitude within the conductive hydrogel for (A) the undeformed baseline and under (B) uniaxial extension ($\lambda_x = 1.15$), (C) bending ($R = 10\ \mathrm{cm}$), and (D) torsion ($\theta = 90°$). The deformed conductive geometry and corresponding changes in electrode position and orientation alter the spatial distribution of the electric field, with localization near the electrodes.

Figure 5. Influence of hydrogel conductivity, σ, on the impedance magnitude, Z, for the undeformed baseline and three representative deformation states: uniaxial extension ($\lambda_x = 1.15$), torsion ($\theta = 90°$), and bending ($R = 10\ \mathrm{cm}$). Impedance decreases with increasing conductivity for all configurations, while the separation of each deformed response from the baseline quantifies the contribution of deformation independently of conductivity.

References

[1] Crandall, H., Schuessler, T., Bělík, F., Fabregas, A., Stults, B. M., Boyadzhiev, A., Zhang, H., et al., 2026, “Cuffless Hemodynamic Monitoring with Physics-Informed Machine Learning Models,” Nat. Commun., **17**(1), p. 6429. https://doi.org/10.1038/s41467-026-72693-1.

[2] Jacobs, I., Lowe, A., Garcia, L., and Zhang, H., 2026, “Advancing Physical Activity Monitoring through Bioimpedance Measurement: A Review,” Prog. Biomed. Eng., **8**(2), p. 022002. https://doi.org/10.1088/2516-1091/ae3671.

[3] Bera, T. K., 2014, “Bioelectrical Impedance Methods for Noninvasive Health Monitoring: A Review,” J. Med. Eng., **2014**, pp. 1–28. https://doi.org/10.1155/2014/381251.

[4] Seward, C., Skolny, M., Brunelle, C., Asdourian, M., Salama, L., and Taghian, A. G., 2016, “A Comprehensive Review of Bioimpedance Spectroscopy as a Diagnostic Tool for the Detection and Measurement of Breast Cancer-Related Lymphedema,” J. Surg. Oncol., **114**(5), pp. 537–542. https://doi.org/10.1002/jso.24365.

[5] Ward, L. C., 2006, “Bioelectrical Impedance Analysis: Proven Utility in Lymphedema Risk Assessment and Therapeutic Monitoring,” Lymphatic Res. Biol., **4**(1), pp. 51–56. https://doi.org/10.1089/lrb.2006.4.51.

[6] Fernandez Schrunder, A., Rodriguez, S., and Rusu, A., 2022, “A Finite Element Analysis and Circuit Modelling Methodology for Studying Electrical Impedance Myography of Human Limbs,” IEEE Trans. Biomed. Eng., **69**(1), pp. 244–255. https://doi.org/10.1109/TBME.2021.3091884.

[7] Sel, K., Osman, D., Huerta, N., Edgar, A., Pettigrew, R. I., and Jafari, R., 2023, “Continuous Cuffless Blood Pressure Monitoring with a Wearable Ring Bioimpedance Device,” npj Digit. Med., **6**(1), p. 59. https://doi.org/10.1038/s41746-023-00796-w.

[8] Ollmar, S., Fernandez Schrunder, A., Birgersson, U., Kristoffersson, T., Rusu, A., Thorsson, E., Hedenqvist, P., et al., 2023, “A Battery-Less Implantable Glucose Sensor Based on Electrical Impedance Spectroscopy,” Sci. Rep., **13**(1), p. 18122. https://doi.org/10.1038/s41598-023-45154-8.

[9] Rodriguez, S., Ollmar, S., Waqar, M., and Rusu, A., 2016, “A Batteryless Sensor ASIC for Implantable Bio-Impedance Applications,” IEEE Trans. Biomed. Circuits Syst., **10**(3), pp. 533–544. https://doi.org/10.1109/TBCAS.2015.2456242.

[10] Kim, J., Oh, S., Avila, R., Shin, H.-S., Banet, M., Wicks, J., Banks, A. R., et al., 2025, “A Compact, Wireless System for Continuous Monitoring of Breast Milk Expressed during Breastfeeding,” Nat. Biomed. Eng., **9**(10), pp. 1645–1655. https://doi.org/10.1038/s41551-025-01393-w.

[11] Qiu, C., Wu, F., Han, W., and Yuce, M. R., 2022, “A Wearable Bioimpedance Chest Patch for Real-Time Ambulatory Respiratory Monitoring,” IEEE Trans. Biomed. Eng., **69**(9), pp. 2970–2981. https://doi.org/10.1109/TBME.2022.3158544.

[12] Sel, K., Osman, D., and Jafari, R., 2021, “Non-Invasive Cardiac and Respiratory Activity Assessment From Various Human Body Locations Using Bioimpedance,” IEEE Open J. Eng. Med. Biol., **2**, pp. 210–217. https://doi.org/10.1109/OJEMB.2021.3085482.

[13] Blanco-Almazán, D., Groenendaal, W., Catthoor, F., and Jané, R., 2019, "Chest Movement and Respiratory Volume Both Contribute to Thoracic Bioimpedance during Loaded Breathing," Sci. Rep., **9**(1), p. 20232. https://doi.org/10.1038/s41598-019-56588-4.

[14] Nescolarde, L., Yanguas, J., Lukaski, H., Alomar, X., Rosell-Ferrer, J., and Rodas, G., 2013, "Localized Bioimpedance to Assess Muscle Injury," Physiol. Meas., **34**(2), pp. 237–245. https://doi.org/10.1088/0967-3334/34/2/237.

[15] Dodde, R. E., Bull, J. L., and Shih, A. J., 2012, "Bioimpedance of Soft Tissue under Compression," Physiol. Meas., **33**(6), pp. 1095–1109. https://doi.org/10.1088/0967-3334/33/6/1095.

[16] Lo Presti, A., Montoya, N. A., Criscuolo, V., Khan, G., Khan, U., Vecchione, R., and Falconi, C., 2023, "Fundamentals of Skin Bioimpedances," Adv. Mater., **35**(33), p. 2302127. https://doi.org/10.1002/adma.202302127.

[17] Veil, C., Müller, D., Walz, S., Schüle, J., Somers, P., Tarín, C., Stenzl, A., and Sawodny, O., 2023, "Enhancing Tissue Impedance Measurements Through Modeling of Fluid Flow During Viscoelastic Relaxation," IEEE Trans. Biomed. Eng., **70**(2), pp. 650–658. https://doi.org/10.1109/TBME.2022.3199468.

[18] Moqadam, S. M., Grewal, P., Shokoufi, M., and Golnaraghi, F., 2015, "Compression-Dependency of Soft Tissue Bioimpedance for *In Vivo* and *In Vitro* Tissue Testing," J. Electr. Bioimpedance, **6**(1), pp. 22–32. https://doi.org/10.5617/jeb.1489.

[19] Mehra, A., Starkoff, B. E., and Nickerson, B. S., 2025, "The Evolution of Bioimpedance Analysis: From Traditional Methods to Wearable Technology," Nutrition, **129**, p. 112601. https://doi.org/10.1016/j.nut.2024.112601.

[20] Hardman, D., George Thuruthel, T., and Iida, F., 2022, "Self-Healing Ionic Gelatin/Glycerol Hydrogels for Strain Sensing Applications," NPG Asia Mater., **14**(1), p. 11. https://doi.org/10.1038/s41427-022-00357-9.